DOI: 10.1002/((please add manuscript number))
Article type: Full Paper

Investigating the role of 4-*tert* butylpyridine in perovskite solar cells

Severin N. Habisreutinger, Nakita K. Noel, Henry J. Snaith & Robin J. Nicholas**

Severin N. Habisreutinger, Dr. Nakita K. Noel, Prof. Henry J. Snaith, Prof Robin J. Nicholas
University of Oxford, Department of Physics, Clarendon Laboratory, Parks Road, Oxford OX1 3PU, United Kingdom
E-mail: h.snaith1@physics.ox.ac.uk, r.nicholas1@physics.ox.ac.uk

Keywords: perovskite solar cells, 4-tert butylpyridine, hole-transporting materials, single-walled carbon nanotubes

1. Introduction

Much excitement has been generated by one of the newest additions to the photovoltaic family - the perovskite solar cell. With the promise to be a technology that can overcome the typical trade-off between high efficiencies and low-cost, the interest in the family of organic-inorganic metal halide materials as absorbers in photovoltaic devices has skyrocketed over the past few years.

In its initial stages, this technology was a mere subset of its ancestor – the dye-sensitized solar cell.[1] By now, however, it has fully grown into its own discreet technology. As in evolution, one can still recognize remnants of its ancestor. One prime example is the presence of a mesoscopic n-type scaffold, which is still used in many variants of the perovskite architecture.[2–4] Because of its very wide absorption in the visible range, the perovskite material was initially thought to act merely as a sensitizing agent in this embodiment. Upon light absorption and charge generation in the perovskite, the electrons are rapidly injected into the mesoporous n-type scaffold through which they are extracted.

A crucial step in the evolution of the perovskite solar cell, was the discovery that the methylammonium lead triiodide perovskite has, in fact, excellent charge transport properties itself. It can therefore also be coated onto an electronically inert scaffold such as Al_2O_3 to both absorb light and transport charge.[5] The obvious next step was the move to planar heterojunction solar cells in both the n-i-p and the p-i-n configuration in which the perovskite absorber does not require a scaffold but is simply sandwiched between a flat n-type and a p-type layer.[6–10] However, while the presence of an n-type scaffold is clearly not a fundamental requirement, currently the best-performing architectures still include a very-thin layer of mesoporous TiO_2 beneath a solid perovskite thin film.[3,4,11]

In this report, we investigate another remnant that has remained in the n-i-p incarnation of the perovskite solar cell without receiving much attention – the hole-transporter additive 4-*tert* butylpyridine (*t*BP). It made its first appearance in a liquid-phase dye-sensitized solar cell (DSSC), where the sensitized TiO_2 electrode was dipped in *t*BP prior to the dye sensitization. As a result, a substantial efficiency improvement was achieved mainly due to an increase in the open-circuit voltage.[12] The initial explanation was that *t*BP adsorbs to the TiO_2 surface where it blocks states which are active as intermediates in the heterogeneous charge transfer thus reducing the dark current.[12] In follow-up studies it was shown that the treatment of the TiO_2 electrode with *t*BP or the addition of *t*BP to the electrolyte shifts the conduction band edge thus yielding an increased V_{oc}.[13–15] This negative shift in the energy bands of TiO_2 results in the reduction of available states for electron injection thus slowing down charge injection, but in addition delaying charge recombination.[16] A reduction of the recombination rate results in a longer charge carrier lifetime which in turn results in an increase in open-circuit voltage.[17] Dürr et al. conclude in their study that *t*BP preferentially adsorbs to defect states on the TiO_2 surface which induce electronic states inside the TiO_2 bandgap and thus are responsible for an increased charge carrier recombination.[18] The adsorption of *t*BP effectively passivates these recombination

centers. As a result, the recombination rate decreases despite a shift of the conduction band toward more negative potentials.[18] In summary, *t*BP affects the electronic properties of TiO_2 by both shifting its conduction band edge and by passivating recombination centers.

A major evolutionary leap for the dye-sensitized solar cell was achieved by Bach et al. who demonstrated that the liquid electrolyte can be replaced by a solid-state organic hole transport material, namely 2,2',7,7'-tetrakis(*N*,*N*-di-*p*-methoxyphenyl-amine)9,9'-spirobifluorene (spiro-OMeTAD).[19] In a follow-up study it was shown that employing *t*BP in the solid-state configuration also has a highly beneficial effect on the solar cell performance.[20] In this case, the addition of *t*BP to spiro-OMeTAD led – as in the liquid-state configuration – to a reduction of the charge recombination rate at the interface and an increase in open-circuit voltage.[20]

Shortly after, the first incarnations of a perovskite solar cell were published, which were both still liquid-state configurations within which the perovskite absorber dissolved within minutes in the electrolyte.[2,21] The seminal breakthrough for perovskite solar cells came when the perovskite absorber was employed in a solid-state configuration using spiro-OMeTAD as hole-transporter, reaching an efficiency of more than 10%, exceeding anything previously achieved with a solid-state DSSC.[5,22] Both of these initial solid-state device reports were based on an n-i-p architecture with spiro-OMeTAD as the p-type layer containing Li-TFSI and *t*BP, which had become indispensable additives to spiro-OMeTAD for solid-state DSSCs. Surprisingly, since then, the best performing n-i-p devices have all employed at least those two additives in their hole-transporting materials.[3,4] Since several reports have pointed out that the reactivity of the lithium salt as well as its hygroscopic nature are detrimental to the chemical integrity of the perovskite,[23–25] a range of approaches have been proposed to remove the need for lithium-doping, for example by pre-oxidizing a fraction of the hole-transporter material.[26,27] Nguyen et al. show that Li-TFSI is not necessarily

required to obtain a high conductivity in spiro-OMeTAD; in contrast, for good solar cell performance *t*BP has proven to be crucial.[26]

Since their first realization, a significant problem in assessing unambiguously the efficiencies of perovskite solar cells has been the presence of hysteresis in the current-voltage scans.[28–30] Ambiguity in determining the efficiency of a device is introduced because the direction and rate of current-voltage sweep impacts the current-voltage curve. The time scales of the observed transient processes suggest that the movement of ionic species are the cause of a change in the charge extraction efficiency depending on scan-rate, scan direction and pre-bias conditions.[30–33] Direct observations of moving ions have been shown by Huang et al.[34,35] A numerical drift-diffusion model by van Reenen et al. suggests that moving ions would produce the experimental results previously described by Tress et al. only with the additional presence of traps active as recombination sites.[36] This result consolidates ionic movement as underlying cause for hysteresis with previous findings according to which trap passivation leads to reduction in hysteretic behavior.[31,37,38] The common factor of all credible analyses of hysteresis is the observation of diminished charge extraction at reverse bias or short-circuit conditions as compared to after a forward biasing step. Independent of the causal factor for this – be it the presence of traps or the reduction of the driving force for charge extraction– improving the charge selectivity of the interfaces is bound to improve steady-state performance of perovskite solar cells.

In this report, we describe a new, likely to be primary, function of *t*BP as an additive to the hole-transporting material in perovskite solar cells, namely, that it improves the charge selectivity of the perovskite-HTM interface thus leading to an improvement in steady-state efficiency. In order clearly pinpoint where and how *t*BP affects the performance of a perovskite solar cell, we deconstruct a typical device layer by layer.

2. Results and discussion

The starting point for this investigation was seeking a strategy to improve the steady-state efficiency of a recently developed new hole-transporter structure in which functionalized single-walled carbon nanotubes extract holes from the perovskite.[24,25] This structure significantly increases the stability and resilience of $CH_3NH_3PbI_3$ solar cells, on one hand due to the absence of the common, hygroscopic dopant Li-TFSI, and on the other, the encapsulating, inert polymer matrix such as poly(methyl methacrylate) (PMMA) capping the device.[24,25] A schematic of a prototypical device is shown in **Figure 1**: the SWNT-PMMA structure extracts holes from the $CH_3NH_3PbI_3$ perovskite absorber, which has been coated onto an alumina scaffold. The n-type acceptor layer is a thin, compact TiO_2 layer, which has been spin-coated onto a transparent fluorine-doped tin oxide (FTO) anode. Copper is used as the cathode collecting the holes from the SWNTs.

In a current voltage sweep from forward bias to open-circuit, the current-voltage characteristics of such a device are obtained, indicating a power-conversion efficiency of 16.2% (**Figure 2 a, Table 1**). However, to avoid any scan rate-dependent ambiguity when determining the power-conversion efficiency of our devices, we measure the stabilized power output (SPO) of a device.[28] In this measurement, the device is held at its initial maximum power-point voltage until the photocurrent stabilizes. For the above device, the photocurrent stabilizes at a significantly lower efficiency value of just 5% (**Figure 2 b**), which means that effectively, this solar cell operates at merely 31% of its scanned efficiency. This fraction of the operational steady-state efficiency compared to the scanned efficiency, we will define as "SPO ratio", which serves a metric for the hysteresis of a device.

While this discrepancy between the efficiency obtained from the current-voltage sweeps and the steady-state efficiency is still present for n-i-p devices with the conventional spiro-OMeTAD hole-transporter, the ratio is typically in the range of 80-90% (**Figure S2**). The spiro-OMeTAD typically contains two additives: Li-TFSI and *t*BP. In assessing what makes spiro-OMeTAD a better HTM with better steady-state performance, one of the variables that is not accounted for and whose role is not fully clear is *t*BP. When the dopant Li-TFSI is added to the spiro-OMeTAD solution, tBP aids the film formation. In the absence of *t*BP, the film formation suffers from dewetting and poor homogeneity. As a result, the overall device performance suffers (**Figure S1, S2, S3**). It has previously been argued that *t*BP increases the polarity of the spiro-OMeTAD solution and thus improves its wetting behavior when spin-coated.[20]

However, investigating the impact of tBP on the performance of devices with lithium-doped spiro-OMeTAD indicates that *t*BP may in fact contribute to an improved steady-state performance as compare to the current-voltage scan performance. The devices in which the spiro-OMeTAD layer contained *t*BP, performed much better both in terms of scanned and steady-state performance. However, due to the aforementioned poorer film quality of the "*t*BP-free" spiro-OMeTAD layer, this difference in performance could be attributed to structural issues of the HTM film rather than an electronic effect of *t*BP.

The dewetting of spiro-OMeTAD without tBP during its deposition is correlated with the presence of Li-TFSI. There is a strategy to improve the charge transport characteristics of spiro-OMeTAD by pre-oxidizing a fraction of it without requiring any additional dopants.[26,27] In this case spiro-OMeTAD forms homogeneous and smooth films independent of *t*BP. Using this strategy, the impact of *t*BP on the steady-state performance becomes evident. While the overall performance is lower compared to lithium-doped spiro-OMeTAD, the addition of *t*BP significantly improves the steady-state performance (**Figure S5**).

These findings led us to investigate the effect of *t*BP in the context of the SWNT-PMMA composite structure. An important aspect of the SWNT-PMMA hole-transport structure is the fact that the layers are deposited sequentially thus allowing the SWNTs to form a dense, interconnected network before the PMMA matrix fills in all the holes of the nanotube mesh and protects the perovskite from moisture degradation. The charge extraction occurs through the SWNTs that penetrate the 300 nm thick PMMA layer.[24] It seemed sensible to investigate the impact of *t*BP on charge extraction by adding it to the SWNT layer, being the electronically active component of the composite. However, even at very low concentrations this led to cluster formation of the SWNTs and degradation of the perovskite. This in turn resulted in very poor device performance. However, while we could not effectively add *t*BP directly to the SWNT solution, we found that we could add it to the embedding polymer matrix.

Corresponding to the previous results, we find that the addition of a small amount of *t*BP to PMMA has a highly beneficial effect on the steady-state performance. The optimum concentration is reached at 20 μl/ml tBP added to PMMA, yielding a device with a stabilized power-output of up to 14.2% (**Figure 3**). The most notable improvements for the scanned performance parameters are an increase in fill factor as well as a significantly higher open-circuit voltage (**Figure 3, Table 1**). The overall most important improvement, however, can be observed in the stabilized power output which improves from around 5% to more than 14%. Accordingly, the SPO ratio is now in the range of 80-90% of the scanned efficiency. This is consistent with the results obtained from conventional devices using spiro-OMeTAD with both additives, Li-TFSI and *t*BP (**Figure S3**).

These results provide further evidence that *t*BP has a beneficial effect on the steady-state efficiency of perovskite solar cells. The question now, is how and through what type of

interaction does *t*BP affects the device performance. We can identify four layers and interfaces with which *t*BP could plausibly interact. Interactions could occur between *t*BP and the PMMA layer, the SWNT layer, the perovskite absorber and the electron-selective TiO_2 layer.

Starting from the top with PMMA polymer matrix which caps the device, it is important to note that this layer does not directly contribute to the charge extraction. Its main role is to minimize shunting paths caused by direct contact between the perovskite absorber and the metal electrode. Thus, it only passively affects charge extraction. Since the *t*BP is added specifically into this layer, we need to investigate how possible *t*BP-PMMA interactions might affect the device performance. Changes in the thickness of the PMMA layer can be excluded, as the change thickness due to the addition of *t*BP at a concentration of around 2 vol% is too small to noticeably impact the performance. In fact, we studied the influence of varying the thickness of PMMA on device performance in order to assess if this could have a significant impact. We found that in order to induce significant changes to the performance, the PMMA matrix has to change by 20-25% thickness, which corresponds to comparable changes in PMMA concentration. Furthermore, the thickness of the PMMA layer correlates in a very specific way to the device performance: the optimum thickness is around 300 nm, thicker layers increase series resistance and reduce the charge collection efficiency, whereas thinner layers lead to increased recombination and reduced shunt resistance (see **Figure S15**).

We also completely replaced the PMMA with polycarbonate and the same improvements of the steady-state efficiency were observed (**Figure S14**). This excludes structure-specific interactions between *t*BP and PMMA. We can therefore conclude that the observed enhancements in device performance occur independent of any possible interactions between *t*BP and PMMA.

The active part of the hole-transporting layer is composed of polymer-functionalized single-walled carbon nanotubes. In order to disperse individual SWNTs and prevent the formation of bundles and clusters, we wrap the SWNTs in a single sheath of P3HT. (Details are described elsewhere[24,25]) Excess P3HT in the solution is discarded during the wrapping process, with P3HT merely present as a dispersing agent wrapped around SWNTs. We disperse the polymer-SWNT-nanohybrids in chloroform prior to deposition.

As mentioned above, we observed that adding *t*BP directly to the SWNT dispersion, resulted in the formation of clusters during the deposition. This could possibly be due to *t*BP having a much higher boiling point than chloroform, which is used as the solvent for this layer. The resulting film is generally quite non-homogeneous.

In order to elucidate whether a specific interaction between *t*BP and the SWNTs could explain the improvement in device performance, we investigated the effect of *t*BP on a range of physical characteristics of SWNT films deposited on glass. Treating an SWNT film with *t*BP does not appear to significantly change the absorption spectrum, the roughness, the conductivity or the energy levels of the SWNTs.

Going back to our initial findings in which the addition of *t*BP to spiro-OMeTAD resulted in an enhancement in the PCE of devices, we can now conclude that this enhancement of device performance actually occurs independent of the hole-transporting material.

The prime candidate for positive interactions with *t*BP is actually the electron-accepting TiO_2 layer. The observed impact of *t*BP on the performance parameters is consistent with previous observations in DSSCs, where the interaction between tBP and TiO_2 surface states results in an increase in voltage and decrease in current.[20,39] However, the TiO_2 interface is deeply buried in this particular solar cell structure. The perovskite absorber is coated onto a 400 nm thick alumina scaffold which it fully infiltrates.[40] Additionally, the

perovskite forms a thick capping layer, which gives the active layer a total thickness of around 1000 nm (**Figure 1 b**). As it is used as an additive to the hole-transporting layer, *t*BP would need to penetrate the entire active layer in order to reach the TiO_2 compact layer.

If the observed effect stems from the interaction between the electron-selective TiO_2 compact layer and *t*BP, treating it directly with *t*BP should presumably yield a similar positive impact on the steady-state efficiency. To test this, we investigated pre-modifying the compact layer by dipping it in undiluted *t*BP, similarly to what has been reported for dye-sensitized solar cells in the past.[12,20] However, the pre-modification of the TiO_2 layer did not show any marked improvement for either scanned or stabilized performance (**Figure S16, S17**). It is possible, however, that the subsequent deposition of the active layer could remove the adsorbed *t*BP from the TiO_2 surface. Assuming that the observed changes in device performance rely crucially on the interaction between *t*BP and TiO_2, the absence of the latter should result in *t*BP being ineffective. We therefore fabricated devices completely without the TiO_2 compact layer.

Consistent with previous results[30,33], after being held at forward bias, the devices without the charge-selective n-type TiO_2 layer still exhibit the rectifying current-voltage behavior of a working solar cell, although with significantly reduced shunt-resistance (**Figure 4 a**). Under steady-state conditions, however, the performance drops very rapidly to a very low PCE (**Figure 4 b**). In contrast, we still observe that the addition of *t*BP to the PMMA layer has an effect on the scanned and, in particular, on the stabilized performance, despite the absence of the TiO_2 compact layer. In addition, its effect is analogous to what we observed in the full devices, which contain the charge-selective n-type contact. In terms of scanned efficiency, voltage and fill factor increase while the photocurrent decreases. The most visible effect is, once again, the much higher stabilized power-output which increases more than six-

fold to around 6.5%. This finding suggests that the beneficial effect of *t*BP on the steady-state performance is not the result of its specific interaction with TiO_2.

The only remaining interface is therefore the one between the perovskite and the HTL. By ruling out interactions at the other interfaces, it appears that *t*BP affects the charge collection efficiency at this interface, especially under steady-state conditions. Considering the observation that the effect of *t*BP occurs independent of the hole-transporting material, this leads to the conclusion that *t*BP interacts specifically with the surface of the perovskite. The following experiments were therefore designed with the aim of elucidating specifically how *t*BP could interact with the perovskite surface, such that it improves the steady-state performance.

In the next step of our investigation, we fabricated devices without selective contacts, in which the perovskite absorber is directly sandwiched between FTO and gold. In order for the perovskite absorber to be similar in its structure to the one used in devices, it was also coated an alumina scaffold. The presence of an alumina scaffold has been shown to directly affect the Fermi level of perovskite, effectively inducing n-doping, which makes these devices slightly asymmetric.[41] We investigated the effect of *t*BP by spin-coating *t*BP in chlorobenzene - at the same concentration as was used in PMMA - onto the perovskite prior to evaporating the gold electrode. The control device was washed with just chlorobenzene to exclude solvent washing effects. The devices were both forward and reverse biased for 10 seconds at ±1.4 V before taking the current-voltage characteristics under light and in the dark.

The *t*BP-treated device, in contrast to the untreated device, shows a much more pronounced rectifying behavior after being forward biased (**Figure 5 a**). The difference is most pronounced in the dark current curves (**Figure 5 b**). In the absence of charge-selective layers, the untreated device behaves like an Ohmic resistor with practically no rectification.

The *t*BP-treated device, however, still shows typical diode behavior. This fundamental change in the current-voltage characteristics of the device in the absence of photogenerated charges cannot be explained by the mere passivation of trap states. Even without charge selective layers, after forward biasing, there remains a driving force for charges to be extracted at their respective electrodes.

By using a Kelvin probe to measure the workfunction of the perovskite surface with and without *t*BP treatment, we see a significant shift of the workfunction from 4.32 eV to 4.93 eV (**Figure S21**). This shift towards a much larger workfunction would imply that there is upward band bending in this region, favoring the charge extraction of photogenerated holes and hampering the extraction of electrons. This type of band bending is indicative of p-doping of the perovskite near this surface region.

In an attempt to explain this phenomenon, we propose that this band bending could be the result of an acid-base reaction between *t*BP and the perovskite. *t*BP is polar and can be considered a moderately strong base. It is therefore possible for it to deprotonate methylammonium at the interface creating a localized negative ionic charge. These immobile, negatively charged ions at the interface would attract mobile holes to compensate for the negative charge in order to maintain the charge neutrality of the crystal. The increase in positive charge carriers in this region would effectively p-dope the perovskite at this interface, resulting in a slight upwards band bending which in turn can facilitate hole extraction, and impede electron transfer (illustrated schematically in **Figure 6**). This possible mechanism would be consistent with both our poling measurements, which show rectification in the absence of charge-selective contacts (**Figure 5**), and the Kelvin probe measurements, which show a shift in work function of the perovskite surface towards larger values (Figure S21). The mechanism proposed would additionally be consistent with the observation that the photocurrent decreases with increasing *t*BP concentration (**Figure S7**), as this can be

explained by the presence of an increasingly strong ionic charge-barrier impairing the charge extraction at this interface.

3. Conclusion

In conclusion, we show that the use of *t*BP as an additive to the hole-transporting material, results in an increase in the steady-state charge-collection efficiency of a perovskite solar cell. This increase in charge-collection efficiency occurs independent of the nature of the hole transporting material used. We propose that this process can occur through the interaction of the *t*BP and the perovskite, which causes the HTL-perovskite interface to become more selective for holes. This study shows that the charge-selective interfaces play a crucial role in efficient steady-state charge extraction. Importantly, the presence of *t*BP appears to have serendipitously induced an effective p-doping of the surface region of the perovskite film, enabling much better diode rectification, even in the absence of charge selective extraction layers in the n-i-p architecture (**Figure 5**). In light of the results which we have presented here, we suggest that all the highest efficiency n-i-p perovskite solar cells which have thus far been reported, are composed of a perovskite layer in which there are n-type, intrinsic, and p-type regions, i.e. “homojunctions”, within the perovskite layer, which are induced by the mesoporous scaffold, on the n-side, and the *t*BP on the p-side. It is therefore likely that focusing on the means to selectively, stably and reproducibly n- and p-type dope the surface regions of perovskite films, may inform the future advancement of this technology.

Experimental Section

Powdered singled- walled carbon nanotubes (SWNTs) produced by the CoMoCAT process, SWeNT CG200, were purchased from Sigma Aldrich. They have a diameter range from 0.7−1.4 nm and a relative purity of 90% as the percentage of carbon that is present as SWNTs. 3.0 mg of rr-P3HT (Rieke Metals Inc., weight-average molecular weight, Mw = 50 000 g mol−1 and regioregularity = 95%) was dissolved in 5.00 mL of chlorobenzene and sonicated in a bath sonicator for 60 min. 2.5 mg of SWNTs was added, as purchased, to the dissolved polymer solution and treated with an ultrasonic probe for 10 min. After the sonication treatment 5 ml of chlorobenzene were added to improve the solubility of the polymer-nanotube-hybrids. The mixture was subsequently centrifuged for 8 min at 10 000g to remove non.functionalized SWNTs and other carbonaceous particles. The precipitate was discarded while the supernatant was recovered. In order to remove the excess polymer according to the solvent extraction technique detailed by Schuettforth et al.,[42] 10 mL of toluene was added. The mixture was then mildly heated for 60 min to induce aggregation of the functionalized SWNTs. The aggregates were then removed by centrifugation (4 min at 16 000 g). This time the supernatant containing excess polymer was discarded and the precipitate was recovered and redispersed in 5 mL of toluene. This mixture was then sonicated for 15 min in the ultrasonic bath to fully redisolve non-wrapped polymers. After the sonication, the mixture was mildly heated for 15 min to induce aggregation and then centrifuged for 4 min at 16 000g. The final pellet consists of 2.0−2.2 mg of polymer-wrapped nanotubes, which are dispersed in 6 mL of chloroform. Immediately prior to spin-coating, the chloroform dispersion was sonicated with an ultrasonic probe for 1 min at low intensity (~10% of amplitude) to break up clusters and bundles.

Solar Cell Fabrication. A glass wafer with a layer of fluorine doped tin oxide (FTO) was first cleaned with detergent and de-ionized water, then with acetone and isopropanol. Thereafter it

was treated for 10 min in O_2 plasma. The electron accepting TiO_2 compact layer was spin-coated (2000 rpm for 60 s) from a mildly acidic (after addition of 12 µM HCl) solution of titanium isopropoxide in anhydrous ethanol and sintered at 500°C. The low-temperature meso-structured scaffold was afterwards deposited by spin-coating (2500 rpm for 60s) from a colloidal dispersion of 50 nm Al_2O_3 nanoparticles in isopropanol followed by drying at 150°C.[6] For the perovskite solution, 440.7 mg/ml of methylammonium iodide (Dyesol) and 257.0 mg/ml of lead(II) chloride (Sigma-Aldrich) were dissolved in dimethylformamide (Sigma-Aldrich) and stirred at 70°C for 30 min. After having cooled down to room temperature, 6 µl/ml of hypophosphoric acid (Sigma-Aldrich) were added to the solution. The perovskite solution was the spin-coated onto preheated substrates and annealed at 100°C for 105 min, followed by 15 min at 120°C. Following this step, the hole transport layer was deposited by spin-coating. For the two-layer structure of SWNT and polymer, first the SWNT layer was deposited dynamically by drop-by-drop spin-coating (3000 rpm for 90 s) of 200 µl. The film was blow-dried with an airgun and let sit to dry at RT for 15 min. PMMA (65 mg/ml in chlorobenzene) was subsequently deposited by spin-coating (2000 rpm for 45 s). 4-*tert*-Butylpyridine (Sigma-Aldrich) was added to the PMMA solution in the range of 0-40 µl/ml. For spiro-OMeTAD HTLs : 96 mg/ml 2,20,7,70-tetrakis-(N,N-di-p-methoxyphenyl-amine)9,9-spirobifluorene (Borun chemicals) was dissolved in chlorobenzene at 90°C. For doping either pre-oxidized spiro-OMeTAD was added at a concentration of 10wt% or for lithium-doping 32 µl/ml lithium bis(tri-fluoromethanesulfonyl)imide (Sigma Aldrich) of a 170 mg/ml solution in 1-butanol were added to the spiro-OMeTAD solution, which was spincoated at 2000 rpm for 60s. Finally, copper electrodes were thermally evaporated onto the HTL.

Current-Voltage Measurements: For measuring the performance of the solar cells, simulated AM 1.5 sunlight was generated with a class AAB ABET solar simulator calibrated to give

simulated AM 1.5, of 100.0 mW cm^{-2} equivalent irradiance, using an NREL-calibrated KG5 filtered silicon reference cel . The current-voltage curves were recorded with a sourcemeter (Keithley 2400, USA). The solar cells were masked with a metal aperture defining the active area (0.0919 cm^2) of the solar cells. Additionally, by removing active material between individual cells on the same glass substrate, single-cell contributions were ensured. Measurements were done in a light-tight sample holder to minimize any edge effects and ensure that the reference cell and test cell are located during measurement in the same spot under the solar simulator.

Kelvin Probe Measurements: Kelvin Probe measurements were taken with a KP Technology Kelvin probe station (KP020 + SPS040). Highly-ordered pyrolytic graphene (HOPG) was used as a reference.

Supporting Information
Supporting Information is available from the Wiley Online Library or from the author.

Acknowledgements
This work was part supported by the ERC StG2011 HYPER, the International Collaborative Energy Technology R&D Program of the Korean Institute of Energy Technology Evaluation and Planning (KETEP) with financial resource from the Ministry of Trade, Industry & Energy, Republic of Korea (no. 20148520011250), and EPSRC.

Received: ((will be filled in by the editorial staff))
Revised: ((will be filled in by the editorial staff))
Published online: ((will be filled in by the editorial staff))

[1] B. O'Regan, M. Gratzel, *Nature* **1991**, *353*, 737.

[2] J.-H. Im, C.-R. Lee, J.-W. Lee, S.-W. Park, N.-G. Park, *Nanoscale* **2011**, *3*, 4088.

[3] W. S. Yang, J. H. Noh, N. J. Jeon, Y. C. Kim, S. Ryu, J. Seo, S. I. Seok, *Science* **2015**, *348*, 1234.

[4] D. Bi, W. Tress, M. I. Dar, P. Gao, J. Luo, C. Renevier, K. Schenk, A. Abate, F. Giordano, J.-P. Correa Baena, J.-D. Decoppet, S. M. Zakeeruddin, M. K. Nazeeruddin, M. Gra tzel, A. Hagfeldt, *Sci. Adv.* **2016**, *2*, e1501170.

[5] M. M. Lee, J. Teuscher, T. Miyasaka, T. N. Murakami, H. J. Snaith, *Science* **2012**, *338*, 643.

[6] J. M. Ball, M. M. Lee, A. Hey, H. J. Snaith, *Energy Environ. Sci.* **2013**, *6*, 1739.

[7] G. E. Eperon, V. M. Burlakov, P. Docampo, A. Goriely, H. J. Snaith, *Adv. Funct. Mater.* **2014**, *24*, 151.

[8] Z. Xiao, C. Bi, Y. Shao, Q. Dong, Q. Wang, Y. Yuan, C. Wang, Y. Gao, J. Huang, *Energy Environ. Sci.* **2014**, *7*, 2619.

[9] P. Docampo, J. M. Ball, M. Darwich, G. E. Eperon, H. J. Snaith, *Nat. Commun.* **2013**, *4*, 2761.

[10] M. Liu, M. B. Johnston, H. J. Snaith, *Nature* **2013**, *501*, 395.

[11] N. Ahn, D.-Y. Son, I.-H. Jang, S. M. Kang, M. Choi, N.-G. Park, *J. Am. Chem. Soc.* **2015**, *137*, 8696.

[12] M. K. Nazeeruddin, A. Kay, I. Rodicio, R. Humphry-Baker, E. Mueller, P. Liska, N. Vlachopoulos, M. Graetzel, *J. Am. Chem. Soc.* **1993**, *115*, 6382.

[13] G. Schlichthörl, S. Y. Huang, J. Sprague, a J. Frank, *J. Phys. Chem. B* **1997**, *101*, 8141.

[14] S. a Haque, Y. Tachibana, R. L. Willis, J. E. Moser, M. Grätzel, D. R. Klug, J. R. Durrant, *J. Phys. Chem. B* **2000**, *104*, 538.

[15] G. Boschloo, L. Häggman, A. Hagfeldt, *J. Phys. Chem. B* **2006**, *110*, 13144.

[16] S. a. Haque, E. Palomares, B. M. Cho, A. N. M. Green, N. Hirata, D. R. Klug, J. R. Durrant, *J. Am. Chem. Soc.* **2005**, *127*, 3456.

[17] R. Kern, R. Sastrawan, J. Ferber, R. Stangl, J. Luther, *Electrochim. Acta* **2002**, *47*, 4213.

[18] M. Dürr, a. Yasuda, G. Nelles, *Appl. Phys. Lett.* **2006**, *89*, 061110.

[19] U. Bach, D. Lupo, P. Comte, J. Moser, *Nature* **1998**, *395*, 583.

[20] J. Krüger, R. Plass, L. Cevey, M. Piccirelli, M. Grätzel, U. Bach, *Appl. Phys. Lett.* **2001**, *79*, 2085.

[21] A. Kojima, K. Teshima, Y. Shirai, T. Miyasaka, *J. Am. Chem. Soc.* **2009**, *131*, 6050.

[22] H.-S. Kim, C.-R. Lee, J.-H. Im, K.-B. Lee, T. Moehl, A. Marchioro, S.-J. Moon, R. Humphry-Baker, J.-H. Yum, J. E. Moser, M. Grätzel, N.-G. Park, *Sci. Rep.* **2012**, *2*, 591.

[23] A. Abate, T. Leijtens, S. Pathak, J. Teuscher, R. Avolio, M. E. Errico, J. Kirkpatrik, J. M. Ball, P. Docampo, I. McPherson, H. J. Snaith, *Phys. Chem. Chem. Phys.* **2013**, *15*, 2572.

[24] S. N. Habisreutinger, T. Leijtens, G. E. Eperon, S. D. Stranks, R. J. Nicholas, H. J.

Snaith, *Nano Lett.* **2014**, *14*, 5561.

[25] S. N. Habisreutinger, T. Leijtens, G. E. Eperon, S. D. Stranks, R. J. Nicholas, H. J. Snaith, *J. Phys. Chem. Lett.* **2014**, *5*, 4207.

[26] W. H. Nguyen, C. D. Bailie, E. L. Unger, M. D. McGehee, *J. Am. Chem. Soc.* **2014**, *136*, 10996.

[27] T. Leijtens, T. Giovenzana, S. N. Habisreutinger, J. S. Tinkham, N. K. Noel, B. A. Kamino, G. Sadoughi, A. Sellinger, H. J. Snaith, *ACS Appl. Mater. Interfaces* **2016**, acsami.5b10093.

[28] H. J. Snaith, A. Abate, J. M. Ball, G. E. Eperon, T. Leijtens, N. K. Noel, S. D. Stranks, J. T.-W. Wang, K. Wojciechowski, W. Zhang, *J. Phys. Chem. Lett.* **2014**, *5*, 1511.

[29] E. L. Unger, E. T. Hoke, C. D. Bailie, W. H. Nguyen, A. R. Bowring, T. Heumuller, M. G. Christoforo, M. D. McGehee, *Energy Environ. Sci.* **2014**, *7*, 3690.

[30] W. Tress, N. Marinova, T. Moehl, S. M. Zakeeruddin, M. K. Nazeeruddin, M. Grätzel, *Energy Environ. Sci.* **2015**, *8*, 995.

[31] N. K. Noel, A. Abate, S. D. Stranks, E. S. Parrott, V. M. Burlakov, A. Goriely, H. J. Snaith, *ACS Nano* **2014**, *8*, 9815.

[32] Y. Shao, Z. Xiao, C. Bi, Y. Yuan, J. Huang, *Nat. Commun.* **2014**, *5*, 5784.

[33] Y. Zhang, M. Liu, G. E. Eperon, T. C. Leijtens, D. McMeekin, M. Saliba, W. Zhang, M. de Bastiani, A. Petrozza, L. M. Herz, M. B. Johnston, H. Lin, H. J. Snaith, *Mater. Horiz.* **2015**, *2*, 315.

[34] Z. Xiao, Y. Yuan, Y. Shao, Q. Wang, Q. Dong, C. Bi, P. Sharma, A. Gruverman, J. Huang, *Nat. Mater.* **2014**, *14*, 193.

[35] Y. Yuan, J. Chae, Y. Shao, Q. Wang, Z. Xiao, A. Centrone, J. Huang, *Adv. Energy Mater.* **2015**, *5*, 1500615.

[36] S. van Reenen, M. Kemerink, H. J. Snaith, *J. Phys. Chem. Lett.* **2015**, *6*, 3808.

[37] A. Abate, M. Saliba, D. J. Hollman, S. D. Stranks, K. Wojciechowski, R. Avolio, G. Grancini, A. Petrozza, H. J. Snaith, *Nano Lett.* **2014**, *14*, 3247.

[38] K. Wojciechowski, S. D. Stranks, A. Abate, G. Sadoughi, A. Sadhanala, N. Kopidakis, G. Rumbles, C. Li, R. H. Friend, A. K.-Y. Jen, H. J. Snaith, *ACS Nano* **2014**, *8*, 12701.

[39] S. Yu, S. Ahmadi, C. Sun, P. Palmgren, F. Hennies, M. Zuleta, M. Göthelid, *J. Phys. Chem. C* **2010**, *114*, 2315.

[40] T. Leijtens, B. Lauber, G. E. Eperon, S. D. Stranks, H. J. Snaith, *J. Phys. Chem. Lett.* **2014**, *5*, 1096.

[41] T. Leijtens, S. D. Stranks, G. E. Eperon, R. Lindblad, E. M. J. Johansson, I. J. McPherson, H. Rensmo, J. M. Ball, M. M. Lee, H. J. Snaith, *ACS Nano* **2014**, *8*, 7147.

[42] T. Schuettfort, H. J. Snaith, A. Nish, R. J. Nicholas, *Nanotechnology* **2010**, *21*, 25201.

Figure 1: Schematic of the employed device architecture and the corresponding SEM micrograph. The solar cell stack is composed of FTO, compact TiO_2, 400 nm of mesoporous alumina which is fully infiltrated by $CH_3NH_3PbI_3$ perovskite, a capping layer of 600 nm

perovskite, a layer of SWNTs, which are embedded in 300 nm of PMMA and finally a copper electrode through which the devices are contacted.

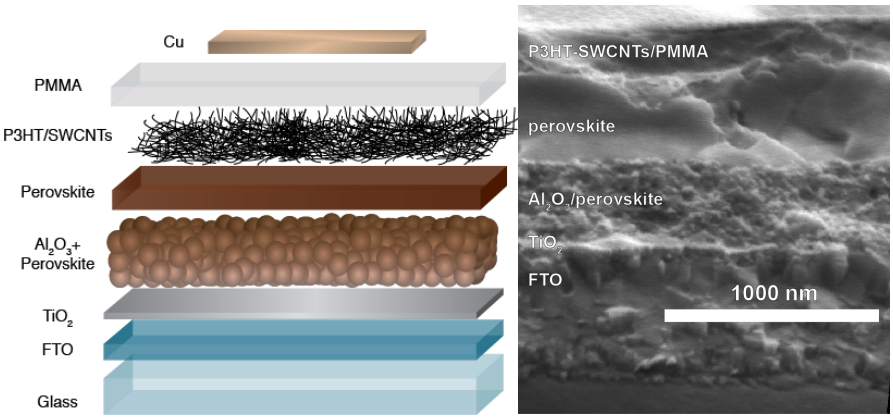

Figure 2: a) Shows the best current-voltage characteristics of a device with the SWNT-PMMA structure, determined by forward-bias to short-circuit voltage scan, yielding an efficiency of 16.2%. b) Shows the corresponding stabilized power output, by measuring the photocurrent of the device at its maximum power-point voltage at 0.80 V, yielding an efficiency of 5.0%.

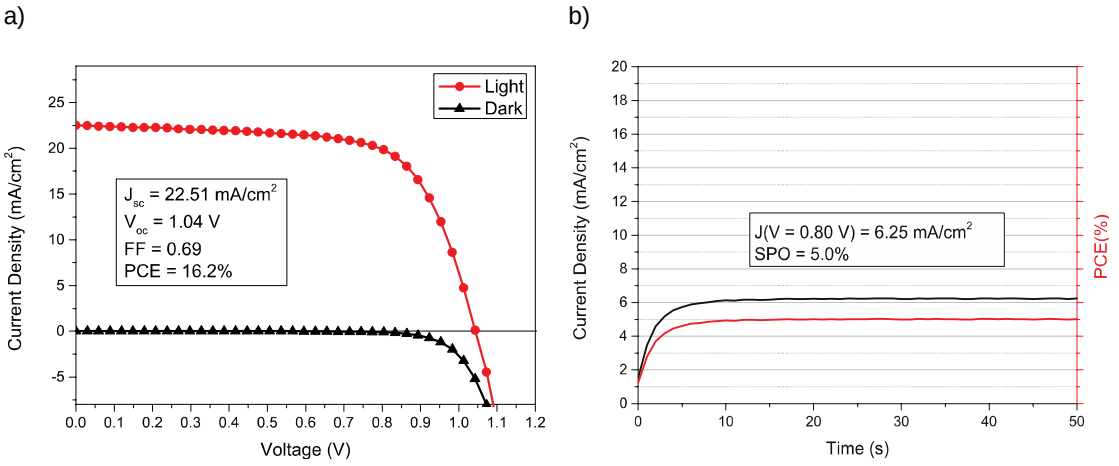

Figure 3: The impact of *t*BP on the device performance of SWNT-PMMA based devices. a) shows the stabilized-power output for a range of *t*BP added to PMMA peaking at 20 □l/ml with a steady-state performance of up to 14.2% b) shows the corresponding SPO ratio for

different *t*BP concentrations, reaching a mean value of around 90% for the optimum concentration c) shows the current-voltage characteristics of a device with *t*BP and d) shows the corresponding stabilized power output at around 82% of the scanned PCE.

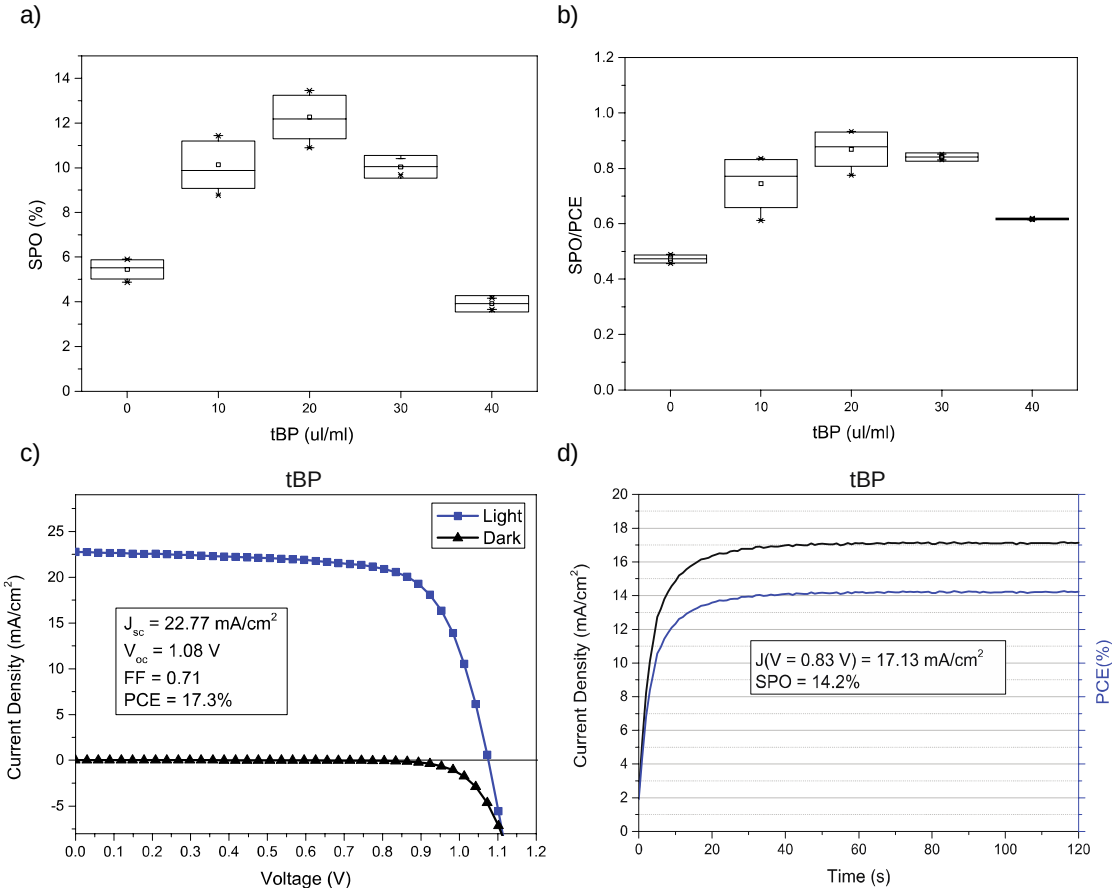

Figure 4: a) Shows the scanned performance of an ETL-free device with and without *t*BP. The changes in the current-voltage characteristics are analogous to devices with an electron-selective TiO_2 compact layer. b) Shows the corresponding stabilized power-output for the two devices, which reveals a much higher SPO for the device containing *t*BP.

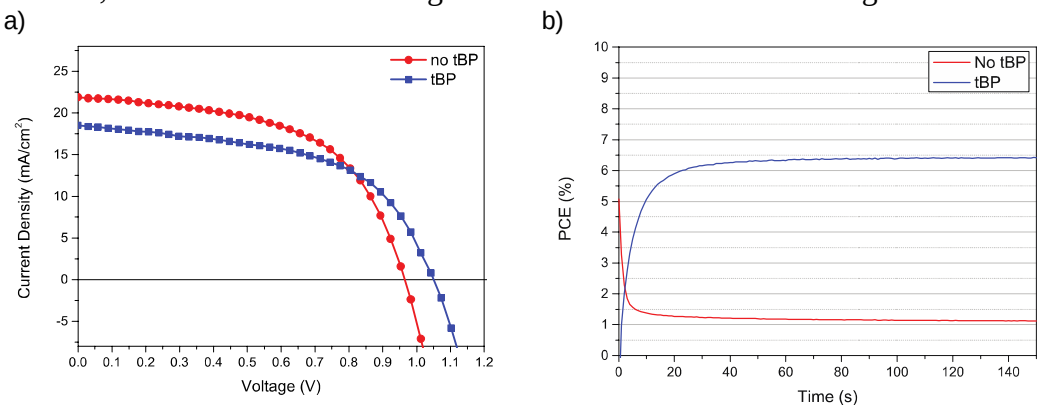

Figure 5: Comparison of *t*BP-treated and untreated perovskite devices without charge selective contacts. a) Shows the current-voltage characteristics for both devices under light when positively biased and when negatively biased. b) Shows the current-voltage scans of the same two devices under the same conditions

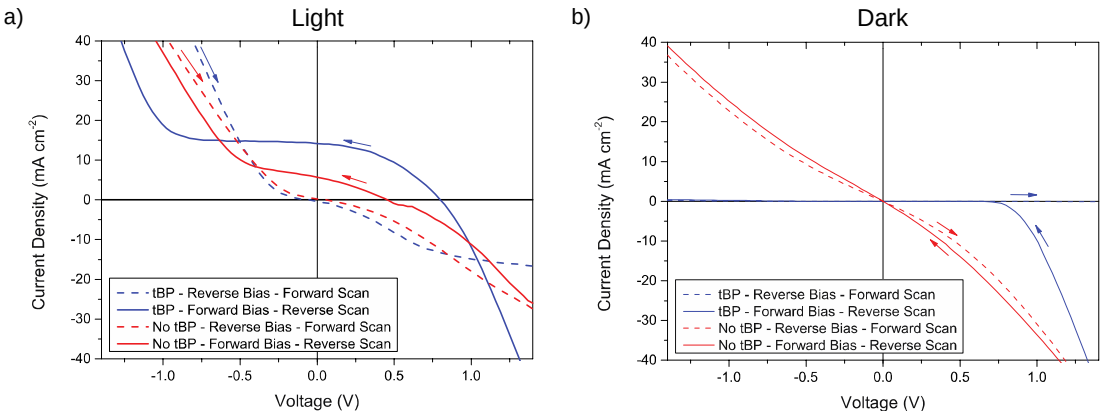

Figure 6: a) Schematic sketch of the proposed mechanism. The *t*BP contained in the hole-transporter effectively p-dopes the perovskite interface by creating a negative ionic charge layer at the interface. In order to maintain the charge neutrality of the crystal, mobile positive charges accumulate in this region effectively p-doping it. This results in band bending favoring the extraction of photogenerated holes over electrons.

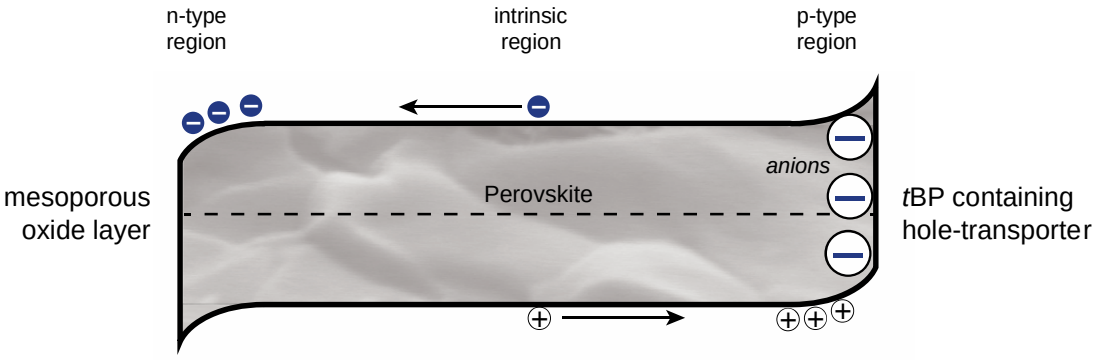

Table 1. Comparison of the scanned performance parameters and the steady-state performance of the devices shown in **Figure 2** and **Figure 3**.

	J_{sc} [mA/cm^2]	V_{oc} [V]	FF	PCE [%]	SPO [%]	SPO/PCE
No *t*BP	22.51	1.04	0.69	16.2	**5.0**	**0.31**
*t*BP	22.77	1.08	0.71	17.3	**14.2**	**0.82**

The majority of hole-transporting materials in n-i-p perovskite solar cells contain 4-*tert* butylpyridine (*t*BP). High power-conversion efficiencies and, in particular, good steady-state performance appear to be contingent on this additive. On the quest for improved steady-state efficiency for a carbon nanotube-based hole-transporter system, we have found that the presence of *t*BP results in an extraordinary performance improvement. By deconstructing a prototypical device layer by layer, we have to conclude that a direct chemical interaction between *t*BP and the perovskite itself must be responsible for the observed performance enhancement. We propose that *t*BP is p-doping the perovskite layer itself and corroborate this with poling and workfunction measurements.

Perovskite solar cells

Severin N. Habisreutinger, Nakita K. Noel, Henry J. Snaith* & Robin J. Nicholas*

Investigating the role of 4-*tert* butylpyridine in perovskite solar cells

Supporting Information

Investigating the role of 4-tert butylpyridine in perovskite solar cells

Severin N. Habisreutinger, Nakita K. Noel, Henry J. Snaith & Robin J. Nicholas**

spiro-OMeTAD Devices with and without tBP

Devices with spiro-OMeTAD as hole transporting material have been prepared. To compare the impact of tBP devices with and without the addition of tBP were investigated, in both cases the spiro-OMeTAD was doped with Li-TFSI. In the absence of tBP, the film formation of the doped spiro-OMeTAD layer is significantly impacted resulting in much worse performance, both in transient scans (figure S1) as well as under steady-state conditions.

Figure S1: performance parameters of devices employing spiro-OMeTAD as hole-transporting material with and without tBP

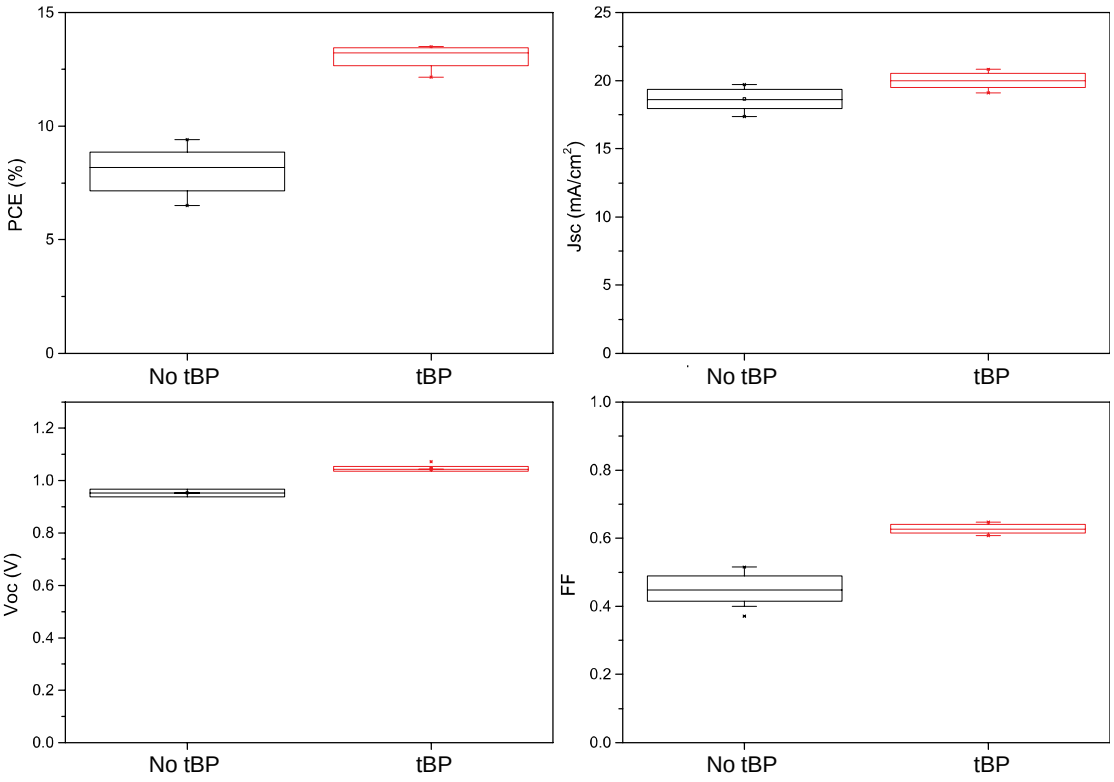

Figure S2: stabilized power-output of devices employing spiro-OMeTAD as hole-transporting material with and without tBP.

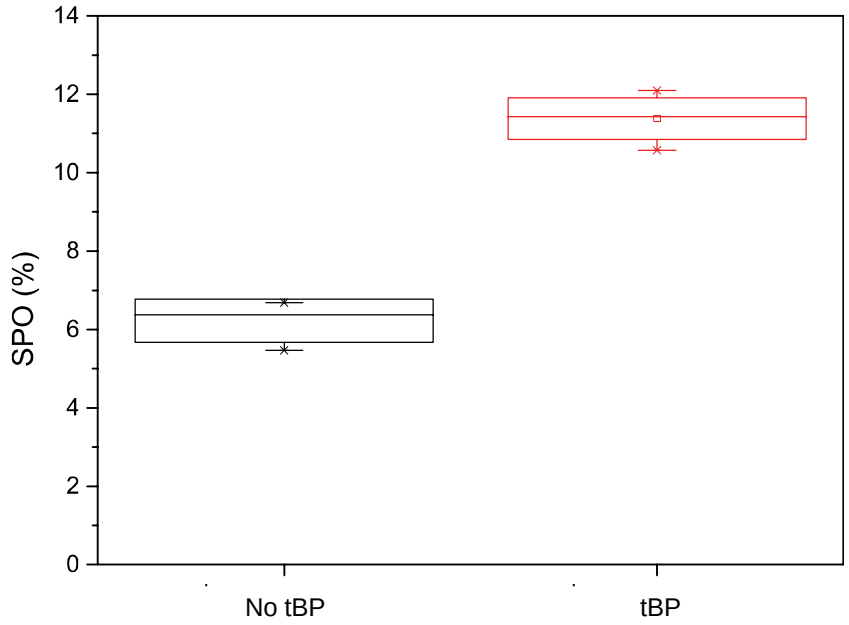

Figure S3: ratio of stabilized power-output to scanned power-conversion of devices employing spiro-OMeTAD as hole-transporting material with and without tBP, showing that tBP leads to a relative improvement of the steady-state performance.

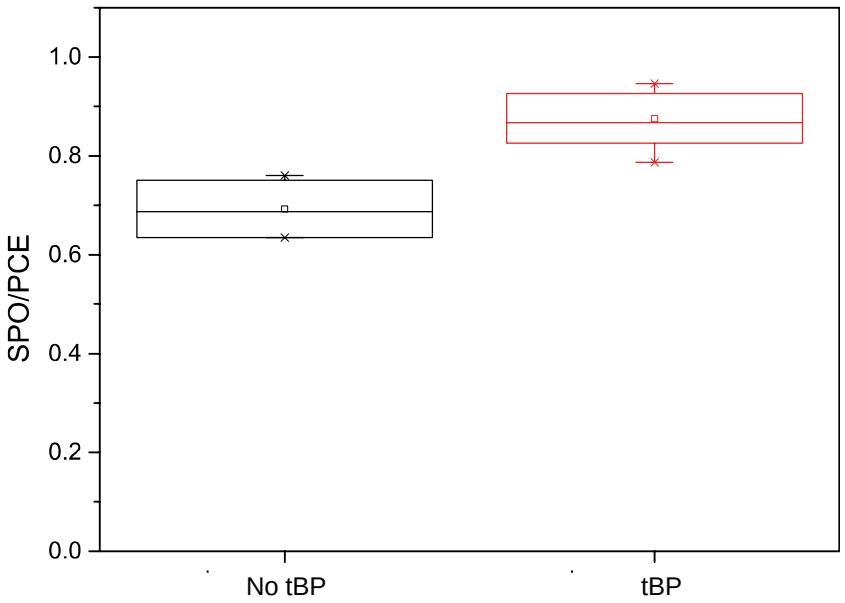

Pre-oxidized spiro-OMeTAD as dopant for spiro-OMeTAD

Figure S4: pre-oxidizing spiro-OMeTAD can be used to increase the conductivity of the hole-transporting material[26,27] without having a detrimental effect on the film formation in the absence of tBP. Here, performance parameters are shown for devices in which the spiro-OMeTAD HTL is doped with pre-oxidized spiro-OMeTAD, with and without tBP. The same trend as in the SWNT-PMMA HTLs can be observed, the addition of tBP leads to an improvement in V_{oc} and FF, while a small decrease in J_{sc} can be observed. However, the net efficiency is still higher for the tBP containing devices.

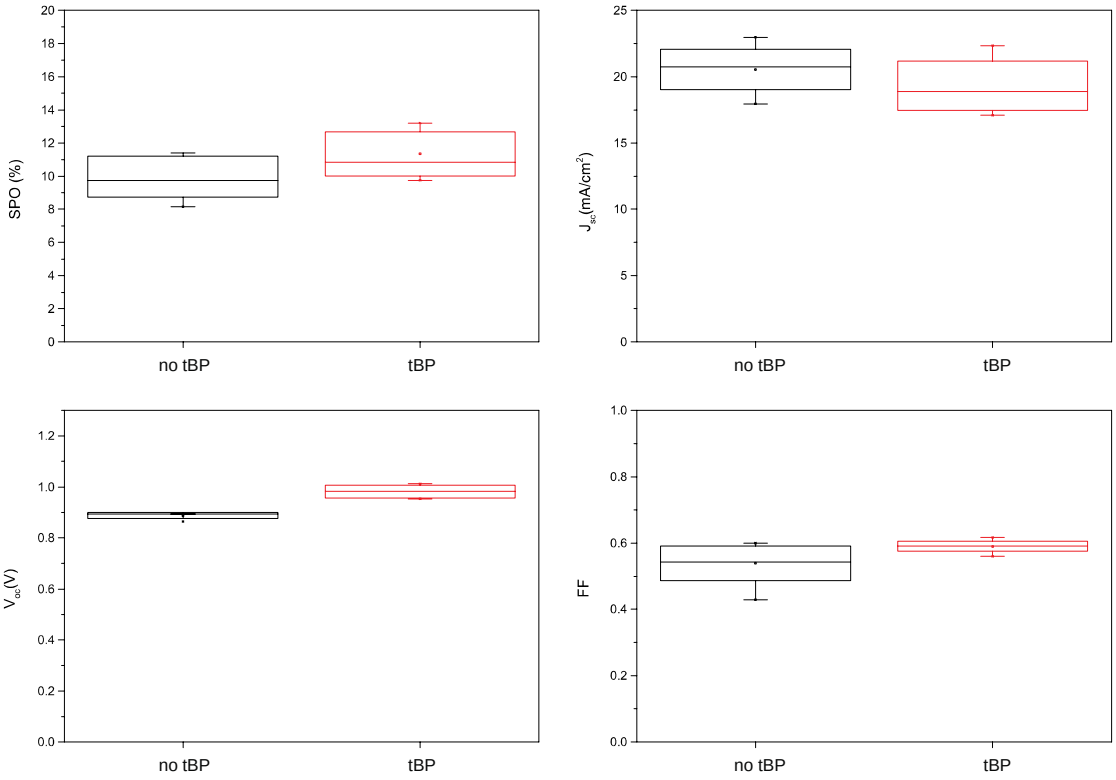

Figure S5: steady-state performance of devices with pre-oxidized spiro-OMeTAD as dopant. The addition of tBP to the HTM results in an improvement of the stabilized power-output by 100%.

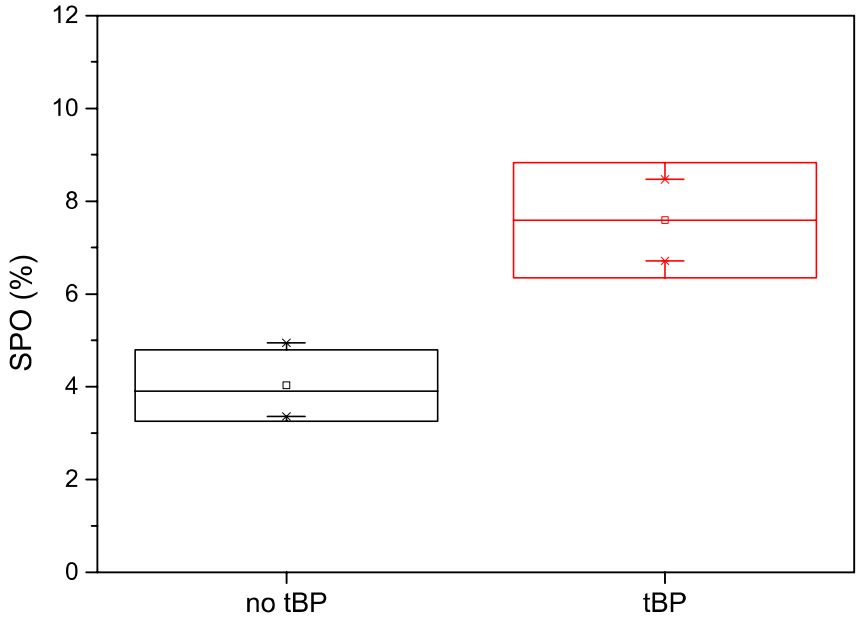

Figure S6: the ratio of the stabilized power-output to the scanned PCE of devices with pre-oxidized spiro-OMeTAD as dopant. The addition of tBP to the HTM does improve the stabilized power-output by 100%.

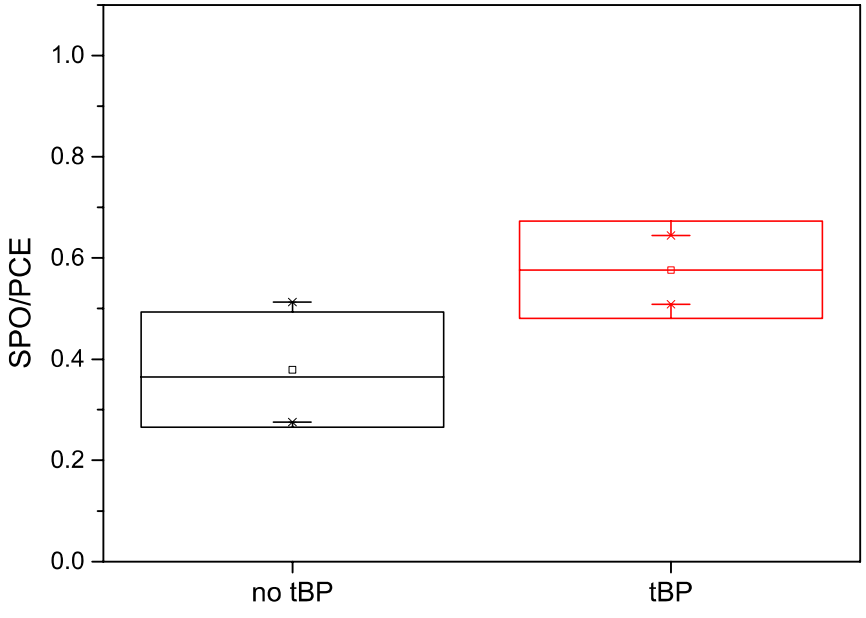

tBP concentration dependence

Figure S7: scanned performance for a batch of devices with different tBP concentrations in the PMMA solution in the range 0 – 40 µl/ml

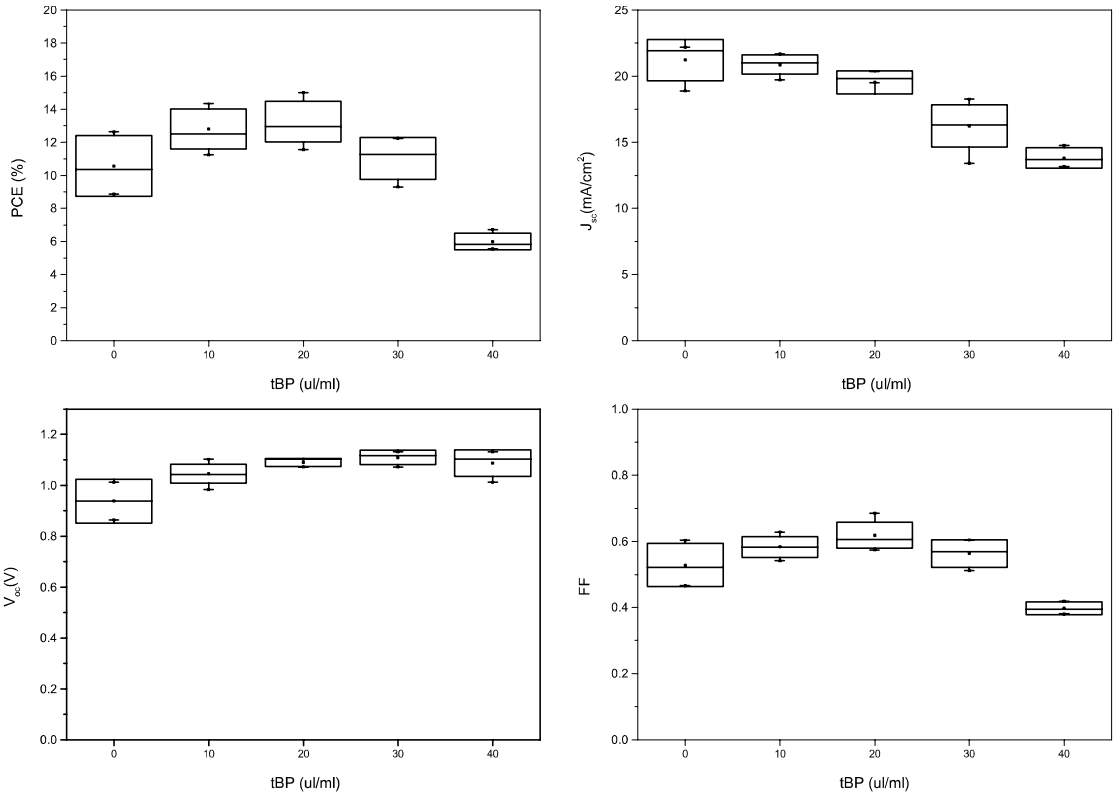

Device statistics

Statistical data of 335 individual devices using the SWNT-PMMA HTM structure, for both scanned performance (figure S8) as well as steady-state performance (figure S9)

Figure S8: scanned performance parameters for 335 devices with and without tBP

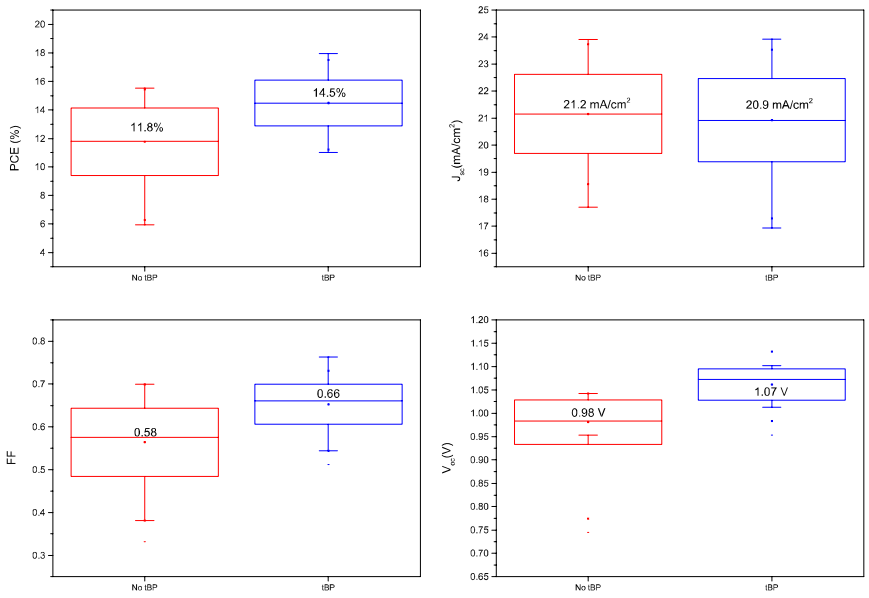

Figure S9: steady-state performance for 145 devices with and without tBP.

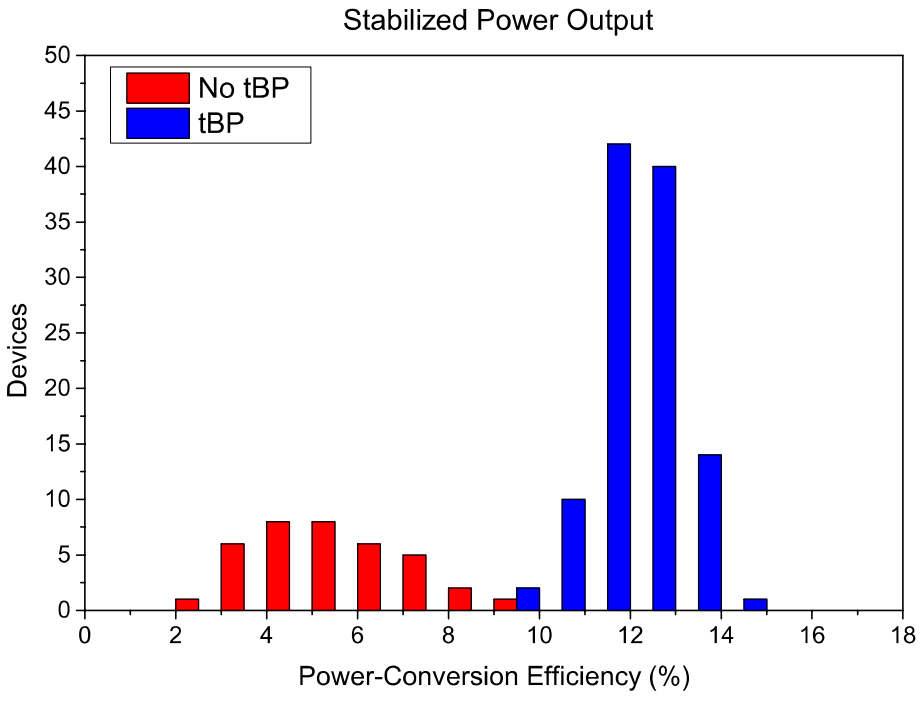

Polycarbonate

Devices in which the insulating polymer poly(methyl methacrylate) (PMMA) has been replaced with polycarbonate (PC) exhibit the same performance improvement upon addition of tBP. In figure S6 and S7, performance of the champion device are shown. In figure S8, S9 and S10, device statistics for polycarbonate devices are shown.

Figure S10: scanned performance for the champion device with tBP-containing polycarbonate as inert polymer matrix on top of the SWNT layer

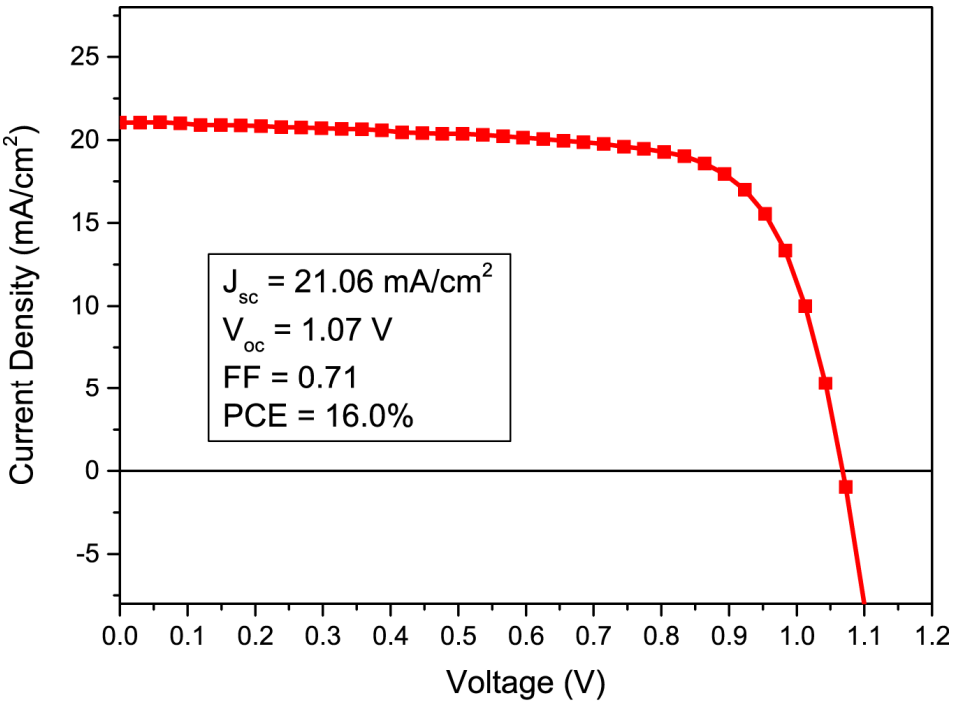

Figure S11: stabilized power-output for the champion device with tBP-containing polycarbonate as inert polymer matrix on top of the SWNT layer

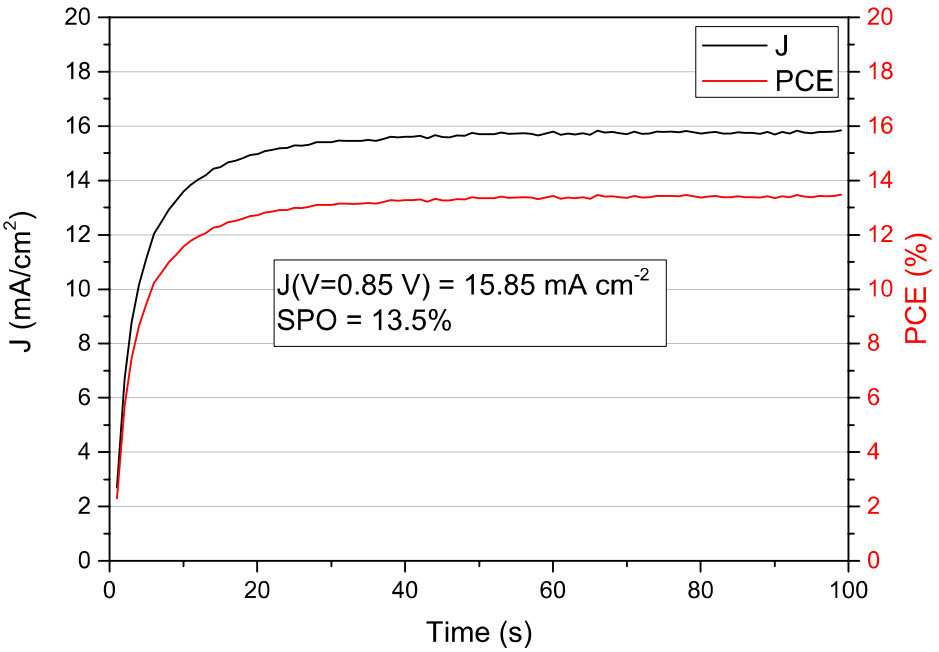

Figure S12: scanned performance for a batch of devices with tBP-containing polycarbonate as inert polymer matrix on top of the SWNT layer

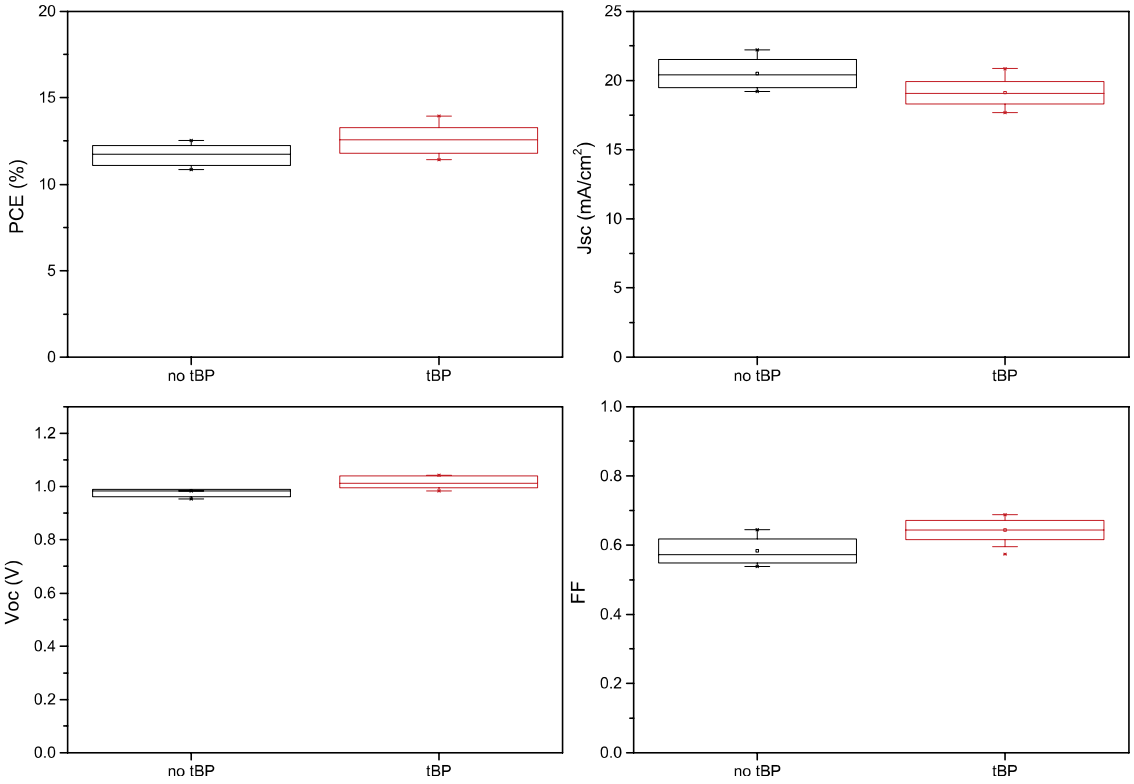

Figure S13: steady-state performance for a batch of devices with tBP-containing polycarbonate as inert polymer matrix on top of the SWNT layer

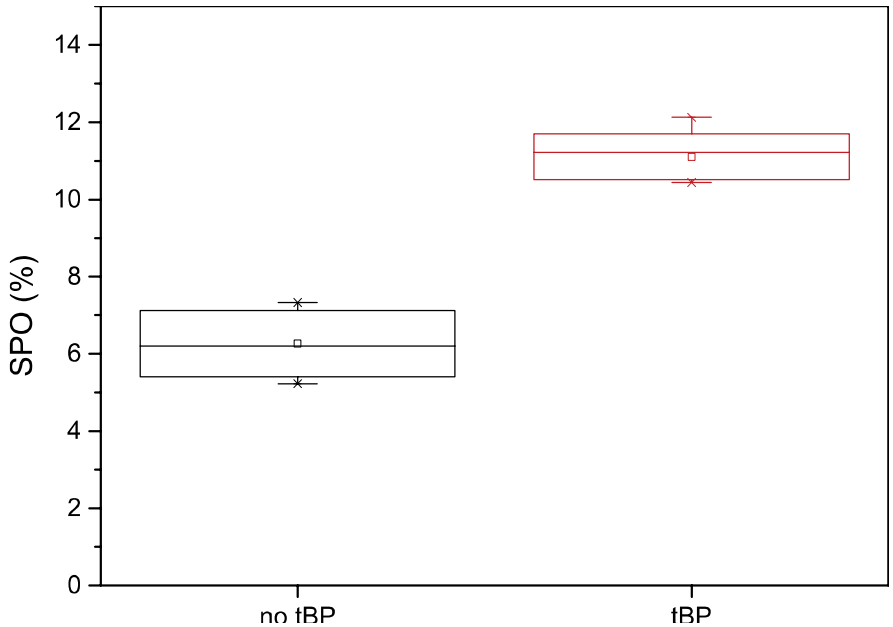

Figure S14: ratio of stabilized power output to scanned power-conversion efficiency for a batch of devices with tBP-containing polycarbonate as inert polymer matrix on top of the SWNT layer, showing the significantly improved steady-state performance in the presence of tBP

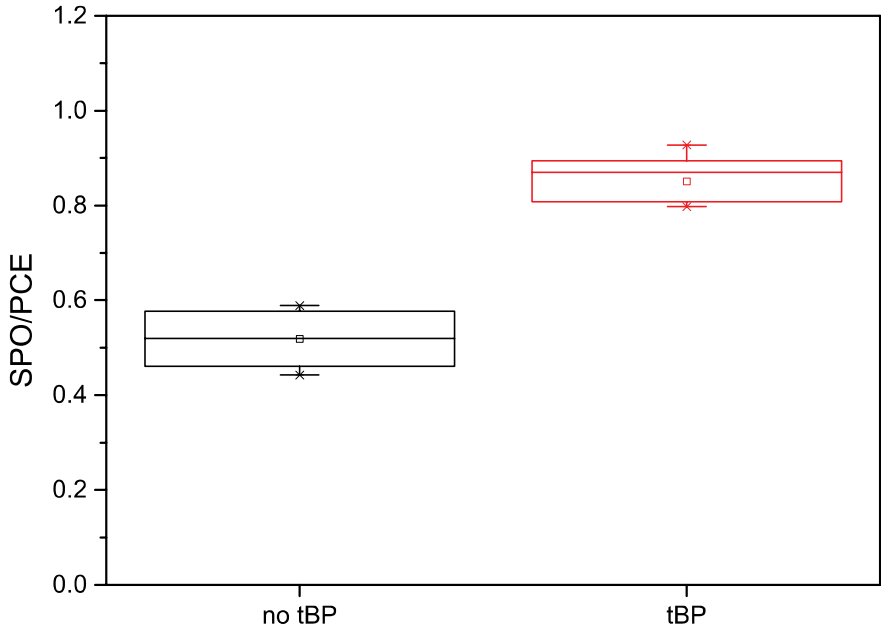

PMMA Thickness dependence

Figure S15: current-voltage characteristics of devices with PMMA layers of different thicknesses. The optimum is reached at a thickness of around 300 nm. Lower thicknesses lead to an increase in recombination and shunting, resulting in lower open-circuit voltages. A thicker layer significantly increases the series resistance hampering charge extraction and thus resulting in very poor device performance

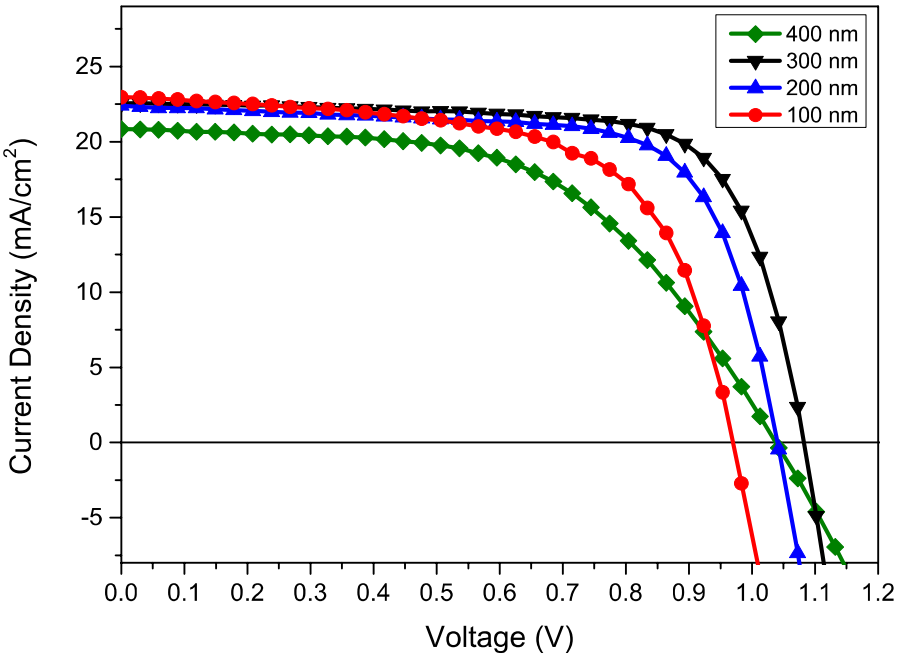

PMMA [nm]	J_{sc} [mA/cm²]	V_{oc} [V]	FF	PCE [%]	R_s [□/cm²]
100	22.96	0.97	0.62	13.81	**2.31**
200	22.39	1.04	0.71	16.53	**2.32**
300	22.36	1.11	0.72	17.75	**2.41**
400	20.83	1.04	0.55	11.91	**10.6**

Table S1: performance parameters of devices with PMMA layers of different thicknesses

TiO_2 premodification with tBP

Figure S16: scanned performance for a batch of devices in which the TiO_2 compact layer was soaked in tBP in order to elucidate whether direct interaction between tBP and the TiO_2 surface is responsible for the performance enhancement. The premodified devices (black) are compared to devices without any tBP (red) and devices where the tBP is included (blue) in the PMMA layer. No improvement can be observed in terms of scanned performance.

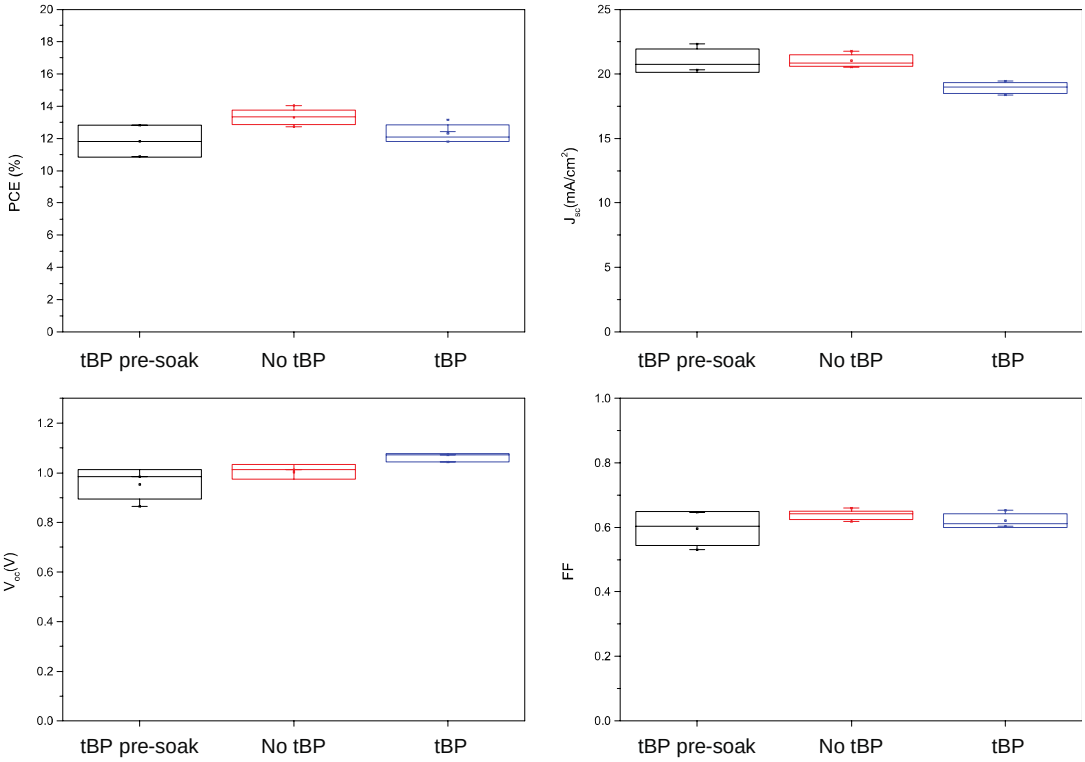

Figure S17: steady-state performance of tBP-premodified devices compared to control devices with PMMA(0) and PMMA(tBP). The premodification has no observable beneficial effect on the stabilized power-output.

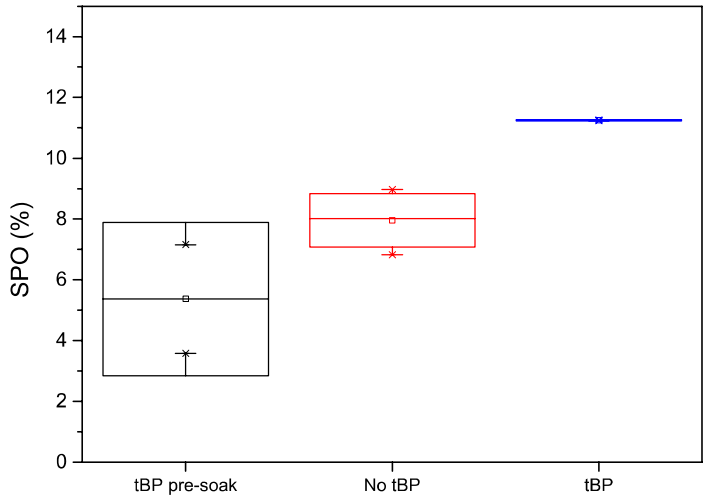

Figure S18: the ratio of steady-state performance to scanned performance of tBP-premodified devices compared to control devices with PMMA(0) and PMMA(tBP). No improvement achievable by pre-modifying the TiO_2 electrode.

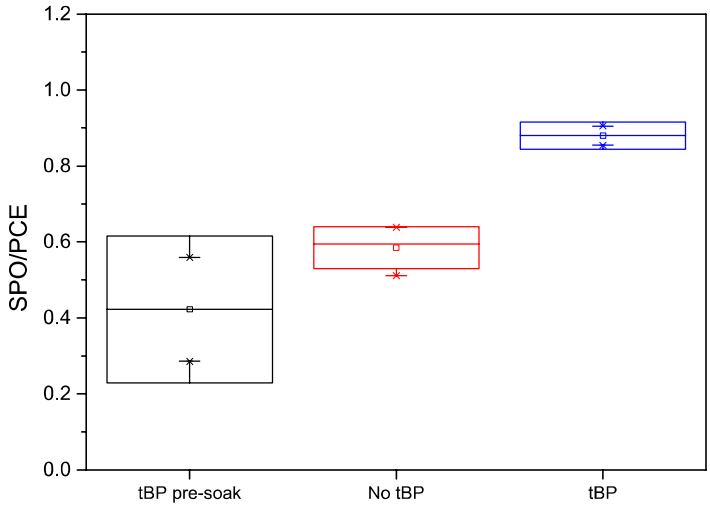

Polystyrene

Figure S19: steady-state performance for devices with non-optimized polystyrene (PS) as insulating matrix. In this case, the addition of tBP also significantly improves the steady-state efficiency.

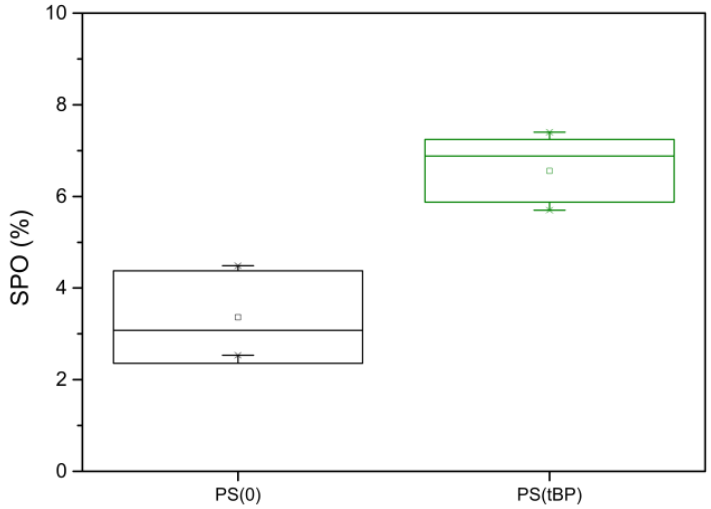

Figure S20: the ratio of the steady-state performance to the scanned efficiency for devices with non-optimized PS as insulating matrix, confirms the systematic reduction in hysteresis when tBP is added to PS

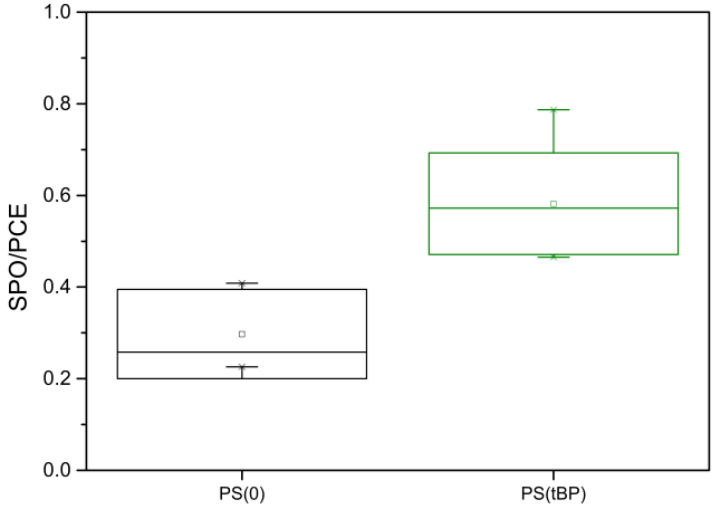

Kelvin Probe Measurements

Figure S21: Kelvin probe measurements of a perovskite film with chlorobenzene treatment (control, red) with a workfunction of -4.32 eV and the same perovskite film after a dilute tBP treatment (tBP, blue) with a workfunction of -4.93 eV. The values were determined with respect to a highly ordered pyrolytic graphite reference at -4.60 eV. The shift towards a larger workfunction indicates an effective p-doping effect induced by the tBP treatment.